ScieRxiv
NOT PEER-REVIEWED
Article

The Sm doping engineering and micromechanisms of a Bi_3YO_6 electrolyte for low-temperature solid oxide fuel cells

Sana Ullah Asif[1,2*], Deyu Zhang[1], Shihong Zhang[3], Muhammad Adnan Qaiser[2], Asif Ali Haider[1], Qingqing Wen[1], Rizwan Raza[4], Muhammad Wasif Ghauri[4], Nusrat Shaheen[2], Shuangbao Wang[1,5*]

[1]Yunnan Key Laboratory of Electromagnetic Materials and Devices, National Center for International Research on Photoelectric and Energy Materials, School of Materials and Energy, Yunnan University, Kunming 650091, Yunnan, China.
[2]Department of Physics, Qilu Institute of Technology, Jinan 250200, Shandong, China.
[3]School of Chemical Science and Engineering, Yunnan University, Kunming 650091, Yunnan, China.
[4]Clean Energy Research Lab (CERL), Department of Physics, COMSATS University Islamabad, Lahore Campus, Lahore 54000, Pakistan.
[5]Electron Microscopy Center, Yunnan University, Kunming 650091, Yunnan, China.

Correspondence to: Prof. Sana Ullah Asif, Prof. Shuangbao Wang, Yunnan Key Laboratory of Electromagnetic Materials and Devices, National Center for International Research on Photoelectric and Energy Materials, School of Materials and Energy, Yunnan University, Kunming 650091, Yunnan, China. Email: sanaullahasif@gmail.com; sbwang0617@ynu.edu.cn

S.U. Asif and D.Y. Zhang contributed equally to this work.

Received: 18 May 2026 | Approved: 28 May 2026 | Online: 28 May 2026

Abstract

In this work, a series of Sm-doped Bi_3YO_6 electrolytes were synthesized via a simple

solid-state reaction route. The optimal composition, $Bi_3Y_{0.80}Sm_{0.20}O_6$ (BYSO), exhibits a maximum ionic conductivity of 4.86×10^{-5} S/cm at 300 °C and 8.1×10^{-2} S/cm at 600 °C in air, as measured using platinum-sputtered pellets. These values significantly surpass those of established low-temperature oxide-ion conductors. Furthermore, the BYSO-fabricated solid oxide fuel cell device exhibited an oxide-ion conductivity of 0.10 S/cm and a high-power density of 587 mW/cm^2 at 550 °C under H_2/air, along with a high open-circuit voltage (≥ 1.00 V). Atomic-scale scanning transmission electron microscopy reveals that the high ionic conductivity stems from an increased concentration of oxygen vacancies due to partial Sm occupation at octahedral interstitial sites within the BYSO lattice, as well as from reconstructed surfaces on the {111} crystallographic planes. First-principles calculations further indicate that the improved conductivity is associated with a narrower band gap and a higher proportion of ionized Sm/Y atoms compared with oxides with other Sm contents.

Keywords: Solid oxide fuel cell, Bi_3YO_6 electrolyte, sm doping, micromechanisms

INTRODUCTION

Depleting fossil fuel reserves and the environmental peril of global warming highlight a strong demand for alternative energy solutions. As a result, there has been a significant increase in scientific and technical interest in various anion conductors. Oxide-ion (O^{2-}) conductors (solid electrolytes) are currently receiving considerable attention due to their applicability in energy systems, particularly solid-oxide fuel cells (SOFCs)[1-4]. One issue with conventional Yttria-stabilized zirconia (YSZ) electrolytes employed in SOFCs is their low ionic conductivity in reduced atmospheres and at low operating temperatures, particularly below 600 °C. Thus, considerable attention has focused on developing alternatives to conventional electrolytes that operate at lower temperatures to address this issue[5]. Popular doped fluorite materials such as $Ce_{0.9}Gd_{0.1}O_{2-\delta}$ and $Ce_{0.8}Sm_{0.2}O_{2-\delta}$ (SDC), as well as perovskite (La, Sr)(Ga, Mg)O_3 oxides, are often considered. However, they face their own set of problems, including chemomechanical stress, electronic conduction arising from chemical reduction, and high reactivity with other cellular components. In addition, they exhibit poor ionic conductivity at 600 °C[6,7]. Therefore, it remains a compelling incentive to explore oxide-ion conductors that exhibit greater conductivities at temperatures lower than 600 °C[8,9].

In solids, oxygen vacancies are the primary source of oxide-ion motion[10]. In recent years, there have been increasing reports of the migration of interstitial oxygen ions and the movement of lattice oxygen ions via knock-on processes. Interstitial oxygen-ion diffusion has been observed in melilite-type oxides, Ruddlesden–Popper phases, hexagonal perovskite derivatives, and scheelite-type oxides[11-14]. In particular, materials that contain bismuth, such as Bi_2O_3, $Na_{0.5}Bi_{0.5}TiO_3$, $CsBi_2Ti_2NbO_{10-\delta}$, and $Bi_{3.9}Sr_{0.1}NbO_{8-\delta}Cl$, have been shown to exhibit high levels of oxide-ion conductivity[15-17]. The Aurivillius phases, BIMEVOX, $Bi_2V_{0.9}Cu_{0.1}O_{5.35}$ (BICUVOX), and $Bi_2V_{0.7}Sb_{0.3}O_{5.5}$ behave the most significant ionic conductivity at low temperatures, compared with other notorious oxide-ion conductors. The crystal structures of $Bi_{3.9}Sr_{0.1}NbO_{8-\delta}Cl$, BICUVOX, and $Bi_2V_{0.7}Sb_{0.3}O_{5.5}$ have a Bi_2O_2 layer that resembles the fluorite type[18-20]. The migration of oxide ions in bismuth-containing materials, such as fluorite-type structured Bi_2O_3, $Bi_{1.4}Yb_{0.6}O_3$, and Bi_3YO_6, occurs through the typical oxygen-vacancy process[21-23]. Introducing oxygen atoms into the interstitial sites of bismuth-containing materials can yield high oxide-ion conductivity.

Electrolytes composed of bismuth oxides possess exceptionally high conductivity at significantly lower temperatures than other oxide-particle-leading solids. Nonetheless, their applications have been limited owing to lower stability, especially in reducing environments (such as H_2); however, deployment at mid-range temperatures (500-700 °C) has been successfully discussed[24,25]. δ-Bi_3YO_6 (BYO) is structurally analogous to δ-Bi_2O_3, as Y^{3+} is isovalent with Bi^{3+} and has the same vacancy concentration with Bi^{3+} in BYO[26]. Abraham *et al.* explained the structural defects and ionic conductivity in BYO using a numerical approach and energy minimization calculations[22,27,28]. Changes in the oxide-ion vacancy distribution were observed clearly, confirming a favored vacancy-pair orientation. Ab initio calculations were used to explore imperfections and trapping effects in the system, and the favored coordination of the dopant cation (Y^{3+}) and its impact on conductivity were established. Recently, ionic conductivity has been studied by adding Niobium and Erbium to

bismuth oxide, but no significant increase was observed[29]. Moreover, the doping of tungsten into bismuth oxide, reported by I. Abrahams *et al.*, resulted in slightly increased total ionic conductivity[27]. Generally, rare-earth elements are a popular option to improve ionic conductance, causing a significant increase in oxide ionic vacancies that directly affect bond interactions, structure, and crystal volume. For example, double rare-earth-substituted bismuth oxide systems (Y/Yb-doped BYO) have been studied, but exhibit reduced ionic conductivity[29]. Recently, Erbium-doped Bi_3YO_6 has been examined, also showing no significant contribution to ionic conductivity[30].

Given the above study, little is known about the optimal conductivity of samarium (Sm)-doped BYO solid electrolytes and the corresponding device performance when used to fabricate a solid-oxide fuel cell under reduced atmospheres and at low operating temperatures. In addition, the micromechanisms by which Sm doping influences the ionic conductivity of BYO require clarification. To this end, $Bi_3Y_{1-x}Sm_xO_6$ (x = 0.0, 0.05, 0.1, 0.2, 0.3) oxide-ion conductors were first prepared, and the optimum oxide-ion conductor was then screened out by testing ionic conductivity in air. A fabricated fuel cell device employing an optimal oxide-ion conductor exhibits high power density under reduced H_2/air atmospheres at low operating temperatures. Enhanced ionic conductance was correlated with Sm doping-modified atomic and electronic structure of the BYO. The results provide detailed insight into how Sm doping modulates the microstructure and properties of BYO, offering a roadmap for designing a high-performance oxide-ion-conducting electrolyte.

EXPERIMENTAL

Sample fabrication

Ceramic samples of $Bi_3Y_{1-x}Sm_xO_6$ (x = 0.00, 0.05, 0.10, 0.20, 0.30) were prepared by the conventional solid-state reaction method Supplementary Figure 1]. Stoichiometric amounts of Bi_2O_3 (Aldrich, 99.9 %), Sm_2O_3 (Aldrich, 99.9 %), and Y_2O_3 (Aldrich, 99.9 %) were used. The raw mixtures were dried, weighed, and ground in ethanol using

a planetary ball mill for 12 h. After that, the powders were dried and sieved. Polyvinyl alcohol (PVA) was then added as a binder to prepare the pellets. Samples were pressed into pellets of 12 mm diameter and 1.5 mm thickness by applying a pressure of 400 MPa. All pellets were annealed at 700 ºC for 4 h at a heating rate of 4 ºC /min to remove binding impurities, then slowly cooled to room temperature. Subsequently, these pellet samples were sintered at 850 ºC for 24 h and cooled to room temperature over 12 h. For electrical measurements, platinum (Pt) was sputtered onto both sides of the pellets to form electrodes using cathodic discharge.

Structural characterizations

X-ray diffraction (XRD) characterization of the required samples was performed on a SmartLab diffractometer (Rigaku Corporation, Japan) using Cu Kα (1.5406 Å) radiation. Data were collected over the $20° < 2\theta < 80°$ range with 0.01° step size. The morphology, composition, and atomic structure of the samples were investigated using a Gemini 500 scanning electron microscope (SEM; ZEISS Corporation, Germany) and a Spectra 300 scanning transmission electron microscope (STEM; ThermoFisher Scientific Inc., USA), which are respectively equipped with energy-dispersive X-ray spectroscopy (EDS). Furthermore, to evaluate oxidation states and confirm constituent elements and oxygen defects, X-ray photoelectron spectroscopy (XPS) was performed for BYO and Sm-doped BYO samples using the ESCALAB 250Xi system equipped with a monochromatic Al $K\alpha$ source ($h\nu = 1486.7$ eV) (ThermoFisher Scientific Inc., USA).

Ionic conductivity measurements

Ionic conductivity was determined by alternating-current (AC) impedance spectroscopy using an E4990A impedance analyzer (Keysight Technologies, USA) coupled with a high-temperature measurement system (Partuloo-1000-DMS) over the frequency range from 20 Hz to 2 MHz at 250 - 600 ºC. Pallets with Pt electrodes on both sides were additionally annealed at 700 °C for approximately 20 min in air to ensure good electrical contact. To confirm measurement accuracy, impedance spectra were recorded

during two consecutive heating-cooling cycles at automatically stabilized, programmed temperatures.

Device fabrication

Commercial $Ni_{0.8}Co_{0.15}Al_{0.05}LiO_{2-\delta}$ (NCAL) powder was used to prepare the fuel cell device. First, the required amount of NCAL powder was weighed and thoroughly mixed with 3 wt% polyvinyl alcohol as a binder. Terpineol was then added to obtain a viscous slurry. The slurry was uniformly coated onto Ni foam. The prepared Ni-NCAL electrodes were dried and then fixed by heating at 140 °C for 30 min before use. The fuel cell device was constructed using optimized $Bi_3Y_{0.8}Sm_{0.2}O_6$ (abbreviated as BYSO in the following context) as the electrolyte in a Ni-NCAL/BYSO/NCAL-Ni configuration. The assembled device was compressed at 200 MPa for 3 min. The cell had a thickness of 1.7 mm and a diameter of 13 mm, giving an active surface area of approximately 0.64 cm^2. The cell was sintered at 600 °C for 2 h to improve mechanical strength. For electrochemical testing, hydrogen (H_2) was supplied to the anode and air to the cathode. The cells were heated to 600 °C at a rate of 5 °C/min under these operating conditions. The flow rates of H_2 and air were controlled between 50 mL/min and 100 mL/min using a mass flowmeter. The current-voltage curves were measured using a SM102 load unit (China). Electrochemical impedance spectroscopy (EIS) of the cell was measured using a CS310M electrochemical workstation (CorrTest, China), at different temperatures (450 °C, 500 °C, and 550 °C). The EIS tests were conducted from 1 MHz to 0.1 Hz at an amplitude of 10 mV.

Theoretical calculations

●In a self-consistent scheme, the structures of $Bi_3Y_{1-x}Sm_xO_6$ (x = 0.0, 0.05, 0.1, 0.2, 0.3) were determined by solving the Kohn-Sham equation, which is based on fundamental concepts. The Perdew-Burke-Ernzerhof (PBE) exchange–correlation function within the self-consistent full-potential linearised augmented plane wave (FP-LAPW) framework was employed for structural optimization. The modified Becke-Johnson potential (mBJ) in the all-electron FP-LAPW-based Wien2k code was used to perform

electronic calculations and improve the accuracy of the results[31,32]. The unit cell comprises the interstitial region and the non-overlapping (muffin-tin) spheres. Within the muffin-tin sphere (MT), the basic functions are expanded in spherical harmonics, whereas in the interstitial region a Fourier series is employed. The MT sphere radii (RMT) for Bi, Y, Sm and O were 2.22, 2.31, 2.4 and 1.89 a.u., respectively. Here, a.u. refers to atomic unit. The energy split between the core and valence states was set to -7 Ry. To verify convergence, the RmtKmax = 8 cutoff parameter was employed, where Kmax is the largest reciprocal lattice vector used for plane-wave expansion, along with Rmt (the minimum MT sphere radius). The most significant vector in the Fourier expansion, Gmax, was set to 12 for the charge density. During self-consistent field (SCF) cycles, we set the energy convergence criterion to 0.0001 Ry and the charge convergence criterion to 0.001 e. To determine the charge density at each self-consistent step, the tetrahedron method was employed to integrate over the Brillouin zone (BZ), which included 159 special k-points in the irreducible wedge and 2000 k-points in the full BZ. A 2 × 2 × 2 supercell was employed for each calculation, which is sufficiently large to minimize interactions. Optical computations were performed for the entire first BZ using a 12 × 12 × 12 mesh.

RESULTS AND DISCUSSION

Phase structure and conductivity of the $Bi_3Y_{1-x}Sm_xO_6$ oxides

To investigate the crystal structure and phase purity of the $Bi_3Y_{1-x}Sm_xO_6$ (x = 0.00, 0.05, 0.10, 0.20, 0.30) ceramic system, XRD analyses were performed first. Figure 1A shows the XRD profiles of all the ceramic electrolytes. The peaks of the undoped BYO sample are well indexed to the JCPDS card (79-0390). As the doping level increases from 0.05 to 0.30, the characteristic peaks of the cubic fluorite structure with space group $Fm\bar{3}m$ (225) persist across the entire compositional range and match well with the standard JCPDS No. 79-0390 of the parent compound Bi_3YO_6[22,30]. Apart from these, no additional peaks are observed in the XRD profiles, indicating a pure parent compound without contamination from secondary phases. Figure 1B shows atomic models of BYO and Sm-doped $Bi_3Y_{1-x}Sm_xO_6$, derived from Rietveld refinement of the diffraction profiles [Supplementary Figure 2], with the corresponding crystal and

refinement parameters in Supplementary Table 1. The results show that BYO occupies four sites in the $Fm\bar{3}m$ cell, namely the 4*a*, 8*c*, 32*f*, and 48*i* sites (Bi/Y, O1, O2, and O3, respectively). This is consistent with a previous study on the defect structure in BYO using total scattering and simulation[22]. With Sm doping, Y at the 4*a* site of Bi_3YO_6 can be substituted by Sm atoms from the same IIIB group, forming $Bi_3Y_{1-x}Sm_xO_6$ oxides. Meanwhile, both lattice parameter *a* and volume *V* exhibit nonlinear positive deviations from Vegard's law as Sm concentration increases. This suggests that shifts in *a* and *V* with concentration are governed solely by the relative sizes of the involved ions (r-Sm^{3+} = 1.079 Å and r-Y^{3+} = 1.019 Å) in the basic replacement mechanism[33]. In addition, the deviation may be attributed to disorder in the oxygen substructure (such as the presence of oxygen vacancies) and the dopant's occupation of the 48*i* site[22,23,34,35].

AC impedance spectroscopy is a powerful technique for examining the electrical transport behavior of various materials. Impedance measurements (Z' *vs.* Z'') were recorded between 250 ºC and 600 ºC for $Bi_3Y_{1-x}Sm_xO_6$ across a range of frequencies. At low temperatures (250 ºC, 300 ºC, and 350 ºC), the plots show a single semicircle and a blocking tail for a given oxide-ion conductor with Pt-sputtered electrodes, as shown in Figure 1C and Supplementary Figure 3A and B. However, at 400 ºC, 450 ºC, 500 ºC, 550 ºC, and 600 ºC, the semicircles fall outside the frequency window; thus, only the blocking tails are observed, as shown in Figure 1D and Supplementary Figure 3C. In this high-temperature range, the grain resistances correspond to the intercept of the lower linear part of the tail. EIS curves were fitted with an R(R//Q)(R//Q) equivalent circuit using ZSimpWin. In this model, the high-frequency R//Q element corresponds mainly to the bulk/ohmic contribution, and the low-frequency R//Q element to electrode polarization. The ohmic resistance was taken from the high-frequency intercept on the real axis, while the polarization resistance was obtained as the difference between the low-frequency and high-frequency intercepts (or equivalently, as the sum of the fitted polarization resistances). These values were then normalized by the electrode area to obtain area-specific resistances[36]. The Arrhenius

plots of ionic conductivity σ for the examined compositions $Bi_3Y_{1-x}Sm_xO_6$ are illustrated in Figure 1E. Generally, the ionic conductivity of oxides increases with temperature. At higher temperatures, rapid oxide-ion dynamics mean that defect trapping and dopant-induced electron-phonon coupling influence conductivity[30].

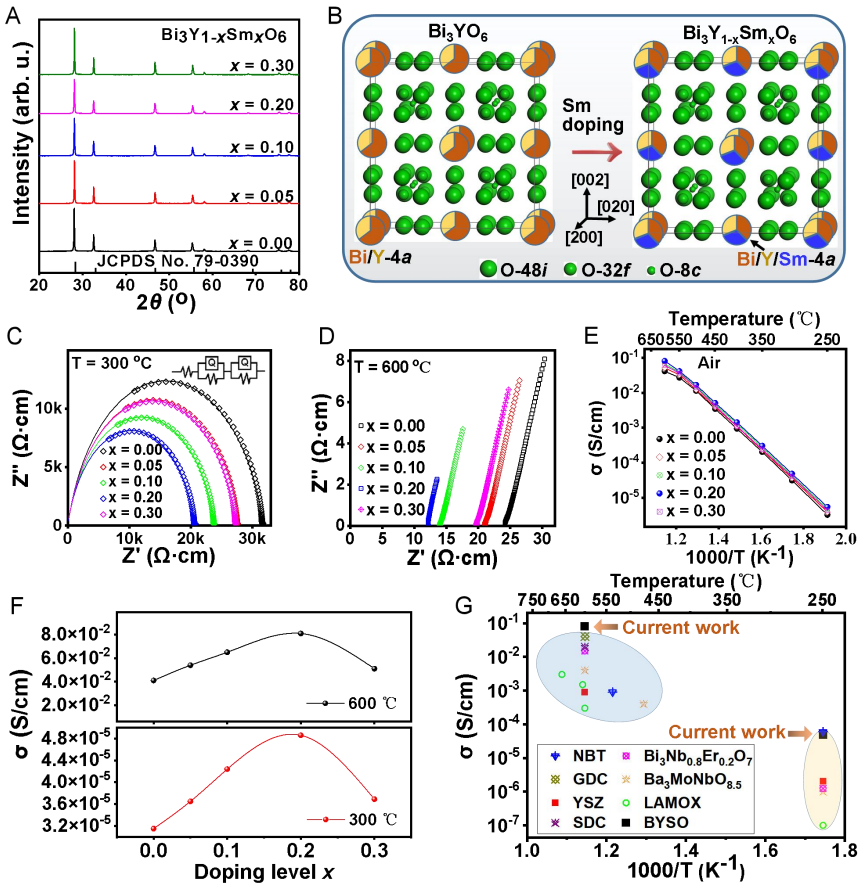

Figure 1. Phase structure and ionic conductivity of the prepared $Bi_3Y_{1-x}Sm_xO_6$ (x = 0.00, 0.05, 0.10, 0.20, 0.30) nanocomposites. (A) XRD profiles; (B) Atomic models of Bi_3YO_6 and Sm-doped $Bi_3Y_{1-x}Sm_xO_6$ derived from Rietveld refinement profiles; (C and D) Exemplary impedance plots at 300 °C with fitted equivalent circuit (inset) and 600 °C in air; (E) Arrhenius plots of total conductivity σ for exemplary BYO and BYSO; (F) Exemplary plots of σ *vs.* doping level x at 300 ºC and 600 ºC; (G) Comparison of oxide-ion conductivities of the current BYSO with other well-known oxide-ion materials.

Figure 1F shows the variation in conductivity of $Bi_3Y_{1-x}Sm_xO_6$ with Sm doping level at

two temperatures, 300 ºC and 600 ºC. Conductivity increases as x increases from 0 to 0.2, then decreases at x = 0.3. The conductivities of BYO at 300 ºC and 600 ºC (σ300 and σ600, respectively) are σ300 = 3.15 × 10^{-5} S/cm and σ600 = 0.041 S/cm, which agree well with previous reports and confirm excellent conductivity for this phase[22,30,37]. In a given temperature regime, optimum conductivity was observed for $Bi_3Y_{0.8}Sm_{0.2}O_6$ (BYSO), with a lower activation energy (ΔE) of 1.09 eV compared to the parent compound BYO, as shown in Supplementary Table 2. The lower activation energy of BYSO is attributable to ion movement among the regular fluorite 8*c* sites, whereby ions from 8*c* sites must pass through two adjacent 32*f* sites to occupy the substitutional 48*i* sites. This phenomenon increases the mobility of ions already present at the 32*f* site, and compositions with higher 32*f*-site occupancy exhibit lower activation energies[27]. In contrast to the lower doped compositions, the x = 0.4 sample showed a pronounced drop in conductivity. This decline is likely caused by the strongest trapping effect and the increased configurational entropy that develop when two similarly sized and highly charged cations Sm^{3+} and Y^{3+} are present in nearly equal proportions at the highest doping level[23]. A comparable sharp decrease in conductivity at high dopant concentration was also reported by Verkerk *et al.* in the Bi_2O_3-Er_2O_3 system[38]. In addition, the greater cation and anion disorder at this composition may restrict oxide ion hopping at elevated temperatures. Strong electron-phonon coupling may further lower the effective defect concentration, which also reduces ionic conductivity[39]. This behavior may also be interpreted in terms of the mobile mixed ion effect, which is commonly associated with the presence of more mobile ions within the sublattice[40]. Figure 1G compares the ionic conductivity of BYSO with other reported oxide-ion conductors. The results show that the current BYSO material system can be utilized and is preferred over well-known oxygen-ion conductors such as Yttria-stabilized zirconia (YSZ)[41], $La_2Mo_2O_9$[42], SDC (0.01 S/cm)[6], GDC[43], $NdBaInO_4$, $Ba_3MoNbO_{8.5}$ and NBTs *etc*[44-46]. for electrical applications, e.g. oxygen separation membranes, gas sensors, and solid oxide fuel cells, due to its enhanced stability and properties.

Device performance of BYSO-based SOFC

To evaluate the electrochemical performance of the BYSO electrolyte, fuel cell experiments were conducted, and open-circuit voltages (OCVs) and maximum power densities (P_{max}) were used to assess the Ni-NCAL/BYSO/NCAL-Ni configuration operated at 450, 500, and 550 °C. Hydrogen was supplied to the anode as fuel, and oxygen to the cathode as oxidant. Figure 2A shows a schematic illustration of the SOFC device. A constant OCV was used to assess the fuel cell's performance. Figure 2B shows the results for the BYSO-based SOFC device, with peak power densities of 587, 447 and 353 mW/cm^2 at operating temperatures of 550, 500 and 450 °C, respectively, which are much higher than those reported for fluorite structures such as BYO, YSZ, SDC, and GDC[13,22,47-56]. Please refer to Supplementary Table 3 for a more systematic comparison of the power density obtained from our work with those reported from other works under similar testing conditions. Furthermore, high OCV values (> 1.01 V) were observed, confirming the absence of short-circuiting. But this does not mean that there is no electronic conduction for this type electrolytes themselves[57]. For instance, BYO can be used as electrodes of capacitor[37,58]. The electrochemical performance of the BYSO was also tested in a reduced H_2/air atmosphere, yielding a small arc with a blocking tail, which can be fitted with a R(RQ)(RQ) equivalent circuit using ZSimpWin software. However, as reported above, for such oxide ion-conducting materials, grain resistance has been inferred from the intercept of the lower linear part of the tail along the *x*-axis [Figure 2C][36]. The ionic conductivity for the BYSO, calculated from the lower linear intercept, was about 0.1 S/cm at 550 °C. The overall ionic conductivity was observed to be greater than 0.01 S/cm, confirming the better performance of the BYSO electrolyte, while keeping in mind that no semiconductor or other nanocomposite is doped to achieve better performance of oxide ion-conducting materials. Results from the EIS spectra confirmed improved electrocatalytic activity and efficient charge-transfer kinetics at the electrode-electrolyte interface, leading to better performance at lower temperatures due to rapid catalytic turnover and low ohmic resistance.

A noticeable drop in ohmic resistance occurred at 550 °C, which tells us the electrolyte works much better at higher temperatures. This high conductivity not only reduces ohmic losses but also helps the cell's electrochemical reactions happen faster. The key reason for this boost is the incorporation of samarium (Sm), which adjusts the oxygen vacancy concentration, improves oxide ion transport, and lowers the energy barrier for charge carriers. As the temperature goes down, both ohmic and polarization resistances steadily rise. That leads to lower ionic conductivity and weaker overall performance. This pattern is typical for fluorite-type oxides, where oxide ion transport is thermally activated—lower temperatures make it harder for vacancies to move and slow down the ORR at the electrode-electrolyte interface.

The increased ionic conductivity could be linked to the uniform, compact, and dense BYSO electrolyte with irregular shapes and well-defined grain boundaries [Supplementary Figure 4] and to the oxygen vacancies [Supplementary Figure 5], which led to faster ionic transport and better electrochemical performance of the BYSO electrolyte. In Supplementary Figure 5, O_{Def} peak shift correspond to oxygen defects, corroborated by the rise in the O_{Def} percentage from 42.8% in BYO to 45.14% in the BYSO electrolyte. Furthermore, Figure 2D and inset show an SEM cross-sectional image of the BYSO device, with transparent electrode and electrolyte interfaces and a dense electrolyte layer, indicating no possibility of gas leakage.

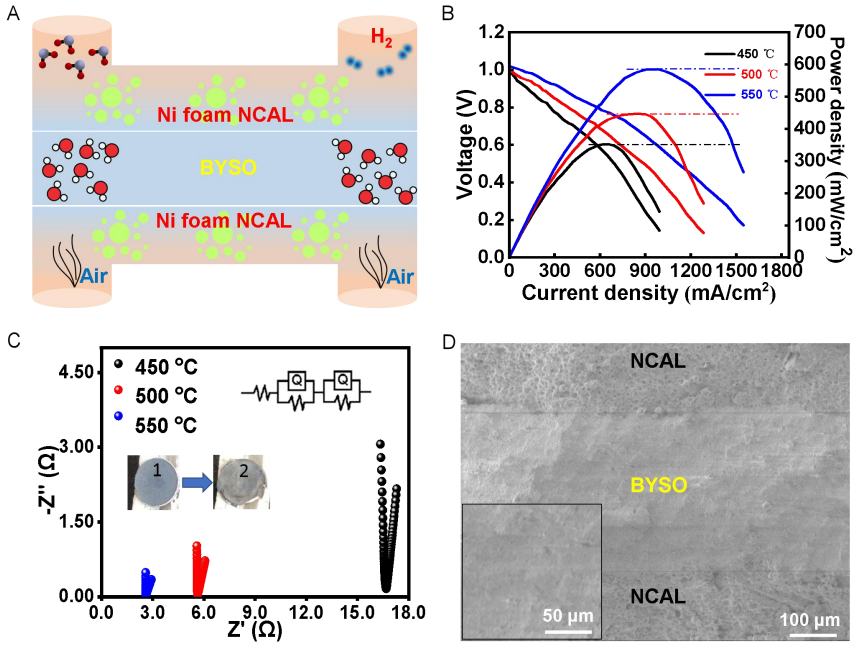

Figure 2. BYSO electrolyte-based performance of the SOFC device at different high temperatures. (A) Schematic setup of the SOFC device; (B) Performance of the SOFC with BYSO electrolyte and NCAL electrodes; (C) Electrochemical spectra of the SOFC device; (D) Cross-sectional SEM micrograph of the fabricated BYSO electrolyte-based device after testing by using coating. Inset in (C) show photo of the cell before testing (labeled as 1) and after testing (labeled as 2). Inset in (D) shows a further zoomed-in view of the BYSO area.

Structural characteristics of BYSO

High-angle annular dark-field imaging (HAADF) in STEM is powerful for determining atomic column positions, while STEM-EDS can distinguish atomic species due to its chemical sensitivity[59,60]. Figure 3A shows an atomic-scale HAADF image of a BYSO particle viewed along the [013] direction. The particle indicated by a red arrow in the low-magnification HAADF image (inset) displays the corresponding morphology. Figure 3B presents EDS maps of Bi, Y, Sm, and O, superimposed on the corresponding HAADF image to reveal the elemental distributions clearly. In the superposition of the main element Bi map and the HAADF image, individual Bi atoms match well with the bright Bi atomic sites (4*a* sites of BYO) in the HAADF image, indicating the reliability of the EDS maps obtained. From the superposition of the Y map & the HAADF image,

the bright atomic sites (4*a* sites) in the HAADF image are also occupied mainly by Y. In addition, an evident Sm occupation at 4a sites is observed in the superposition of the Sm map and the HAADF image. The Sm occupation with Bi and Y at 4*a* site agrees well with the atomic model of $Bi_3Y_{1-x}Sm_xO_6$ [Figure 1B] revealed by Rietveld refinement analysis of XRD profiles [Supplementary Table 1]. As seen in the superposition of the O map and the HAADF image, O can be distributed between the bright atomic layers of cations or within the atomic layers of cations, which is consistent with the [013]-oriented atomic models shown in Figure 3C and D. In other words, Bi/Y/Sm located at position 4*a* and partially O located at position 48*i* occupy the same (002) atomic layers (abbreviated as Bi/Y/Sm/O-48*i* planes), while O located at positions 8*c*, 32*f*, and the remaining 48*i* are distributed in the middle of the cation layer (abbreviated as O-8*c*/32*f*/48*i* planes). It should be noted that some O vacancies may be clearly observed in the superposition of the O map and the HAADF image, consistent with XPS [Supplementary Figure 5] and a previous study[22]. It is seen from Supplementary Figure 5 that the energy difference ΔE between O_{Lat} and O_{Def} is 1.72 eV for BYO, and is 1.56 eV for BYSO. Thus, the difference in ΔE between BYO and BYSO is negligible. Larger area of O_{Def} peak in the BYSO than that in the BYO is associated with broader O_{Def} peak of BYSO. Again, the enlarged HAADF image corresponding to atomic models of Figure 3C and D highlights the distribution characteristics of Bi, Y, Sm and O on the (002) planes, as shown in Figure 3E.

To further elucidate the characteristics of elemental distribution on the (002) planes, detailed line profile analyses were performed on Bi/Y/Sm/O-48*i* planes and O-8*c*/32*f*/48*i* planes of the BYSO particle. Figure 3F shows the integrated line intensity profiles of Bi, Y, Sm, and O, together with the corresponding HAADF contrast, extracted from a local Bi/Y/Sm/O-48*i* plane (inset). Following the line profile of atomic columns in the HAADF image, the elements Bi, Y, Sm, and O exhibit correlated intensity variations at specific bright sites, indicating a consistent atomic distribution with the atomic model. However, partial Sm intensity peaks are located between the peaks of the Bi, Y, and O line intensity profiles, implying a special Sm occupation in

the BYSO crystal structure. Figure 3G shows the integrated line intensity profiles of O and the corresponding HAADF contrast from a local O-8*c*/32*f*/48*i* planes (inset). As shown, there is a pronounced variation in O intensity, indicating apparent O vacancies at the 48*i* sites in the $Bi_3Y_{0.8}Sm_{0.2}O_6$ crystal structure. A possible reason is that a finite number of oxide ions occupy the 48*i* site, while the 8*c* and 32*f* sites are occupied to a significant extent[22].

The schematic in Figure 3H offers a potential explanation for the distinct occupation of Sm at the 4a sites in Figure 3F. An arresting feature of the BYSO atomic model is that an octahedral interstitial position occupied by cations is located at the centre of the structure. A Frenkel pair, or Frenkel defect, occurs in a crystal lattice when an atom leaves its lattice site and becomes an interstitial, creating a vacancy at its original site due to thermal vibrations[61-63]. Imagine that in the BYSO lattice, there is a probability for Sm to occupy octahedral interstitial positions because of the complex atomic coordination environment, forming a Frenkel pair. The pair will recover in most cases. However, if the vacancy is filled by surrounding cationic ions and then diffuses away, a Sm atom shifted into an octahedral position will be caged and survive for a relatively longer period. Although unlikely, it is still possible in thermodynamic statistics that a small quantity of caged Sm-interstitials in the crystal lattice is due to (local) thermal fluctuations. The [200] orientation of the BYSO atomic model will transform into the [130] orientation after rotating 18.43° along the [002] axis. At this point, the Sm atom in the octahedral interstitial is located in the middle of the two cation positions, which well explains the EDS observation results of Figure 3F. On one hand, the increase in octahedral Sm interstitials must generate a higher vacancy concentration in the BYSO crystal lattice, thereby leading to increased ability of O diffusion. On the other hand, the octahedral Sm interstitials may be used to explain the expansion of the cubic lattice parameter by considering Sm ions on the site to be the octahedral interstitial of a Frenkel defect. As the occupancy of this site increases, one would expect an increase in the local lattice distortion, resulting in a larger lattice parameter than in Bi_3YO_6.

Consequently, the above findings well explain the increased conductivity and lattice expansion of BYSO compared to those of BYO.

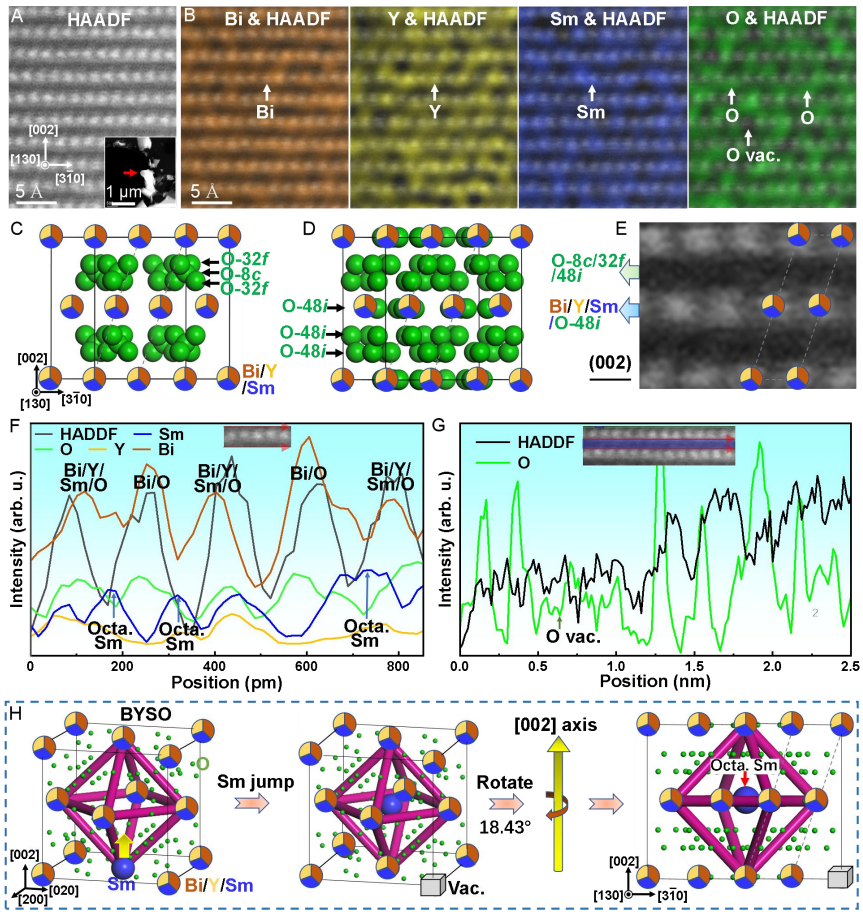

Figure 3. Atomic-scale structure of the BYSO sample. (A) and (B) [013]-oriented HAADF image and corresponding EDS elemental mappings; (C)-(E) [013]-oriented atomic models and corresponding HAADF image highlighting two different atomic layers of Bi/Y/Sm/O-48*i* layer and O-8*c*/32*f*/48*i* layer in the Fm$\bar{3}$m unit cell; (F) and (G) Concentration variations of elements from two different atomic layers (red arrow overlaid areas in the insets) of the unit cell; (H) Schematic illustration of proposed formation mechanisms for the octahedral Sm and vacancies. vac., vacancies; octa., octahedral.

Based on the results shown in Figure 3, Figure 4 further illustrates possible changes in the O ion coordination environment within the BYSO unit cell after the formation of

Sm ion-related Frenkel defects. On the one hand, Sm ions entering the octahedral interstitial positions of BYSO will introduce Sm vacancies. On the other hand, the former octahedral interstitial Sm can also cause the nearest neighbor 48*i* O atom ($d_{\text{Sm-O-48}i}$ = 1.388 Å) to diffuse out of the unit cell first [Figure 4A]. At the same time, some 32*f* O ions ($d_{\text{Sm-O-32}f}$ = 1.758 Å) and 8*c* O ions ($d_{\text{Sm-O-8}c}$ = 2.364 Å) adjacent to the octahedral interstitial Sm ions will also diffuse outside the unit cell [Figure 4B and C]. The main reason for the external diffusion of these O atoms is that octahedral interstitial Sm ions occupy the positions of these original oxygen ions. The outward diffusion of O ions will ultimately result in the formation of a certain number of O ion vacancies around the octahedral interstitial Sm ions [Figure 4D]. It is worth mentioning that the externally diffused O ions will enter the surrounding normal BYSO unit cells, forming free O ions that are weakly coordinated with the surrounding cations [Figure 4E]. Obviously, compared to O ions coordinated around cations, free O ions are more likely to move in the lattice of BYSO under the action of an electric field. Therefore, in addition to Sm ion vacancies, freely moving O ions can also increase the conductivity of the sample to a certain extent. Here, it is worth pointing out that theoretical calculations of the oxygen vacancy formation energy, interstitial oxygen formation energy, and the density of states explaining the change in oxygen ionic and electronic conductivity are valuable and will be considered in future work.

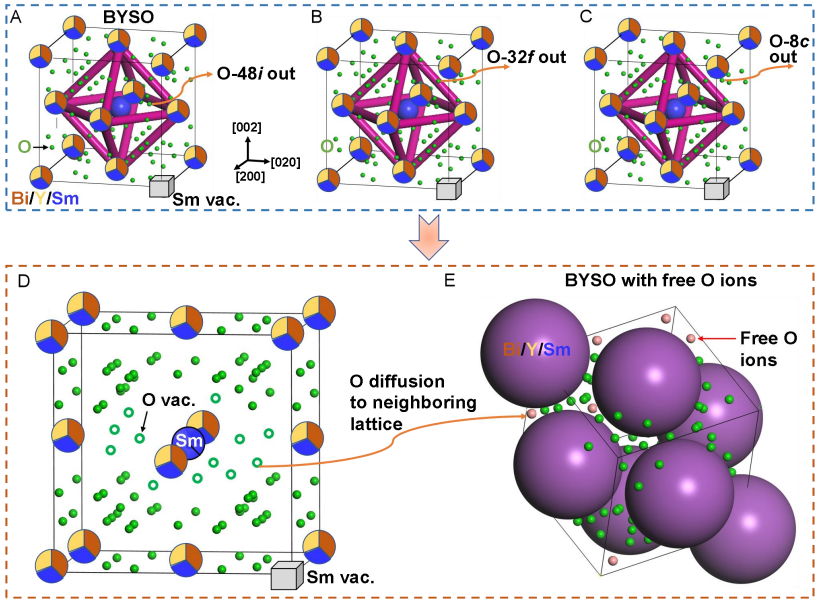

Figure 4. Schematic view showing the potential effect of octahedral interstitial Sm on the surrounding O ions in the BYSO. (A)-(C) Octahedral interstitial Sm induced outward diffusion of neighboring O ions; (D) O vacancies formed around Sm; (E) Formation process of free O ions.

STEM-HAADF and EDS were further used to characterize the surface structural features of the BYSO sample, as shown in Figure 5. Figure 5A shows a typical surface structure at the atomic scale of a particle observed along the [110] zone axis, in which some zigzag surfaces are observed. Indexed fast Fourier transform (FFT) image in the bottom-right inset highlights that the zigzag surfaces belong to the {111} crystallographic family. Growth of the BYSO is expected to occur via lattice stacking along close-packed planes[64]. Figure 5B shows an intensity line profile from the red rectangle overlaid area in Figure 5A. Careful measurement shows that an interplanar spacing of 0.327 nm is consistent with the $d_{(111)}$ value of the BYO crystal (JCPDS No. 79-0390). Figure 5C is the corresponding EDS elemental mappings of Figure 5A, where the Bi, Y, Sm, and O elements are observed to distribute throughout the particle. Nevertheless, the concentration line profiles [Figure 5D] show some characteristic Bi-rich-O lean-Bi/Y/Sm-O lean-Bi-rich surface layers at $\{111\}_{BYSO}$ crystallographic planes. In other words, there is an apparent O deficiency at around a 2-nm-thick surface area of the BYSO particle. It is expected that the generation of O deficiency at the

surface area is closely related to the interaction of Sm, Y, and O at the surface area. Figure 5E shows an enlarged surface area of Figure 5A, in which some lattice with bright contrast corresponds to the mixed Bi/Y/Sm columns according to the atomic model of the BYSO. This is because in the HAADF-STEM image, the contrast of atomic columns is known to be proportional to the atomic number $Z^{1.7–1.9}$[65]. Generally, the atomic number of the elements in the BYSO is the order of Bi (83) > Sm (62) > Y (39) > O (8). It is therefore difficult to observe the O atoms in the HAADF image due to its too small atomic number relative to those of the Bi, Y, and Sm. Close observation of Figure 5E reveals apparent surface reconstruction according to some extraordinary bright atomic contrast of the {111} crystal planes. The brighter atomic contrast of the {111} crystal planes means there is more Bi enrichment in the mixed Bi/Y/Sm columns, which agrees well with the analysis of the EDS concentration line profiles shown in Figure 5D. That is to say that more Bi atoms might replace original Y/Sm sites in the BYSO structure, resulting in the Bi-enriched Bi/Y/Sm columns, as schematically shown in Figure 5F. Here, it can be concluded that the Bi-rich-O lean-Bi/Y/Sm-O lean-Bi rich structure on the surface layer of $\{111\}_{BYSO}$ crystal planes contributes to the increased O vacancies and thus electric conductivity. This further confirms the presence of O vacancies, as revealed by the XPS results shown in Supplementary Figure 5.

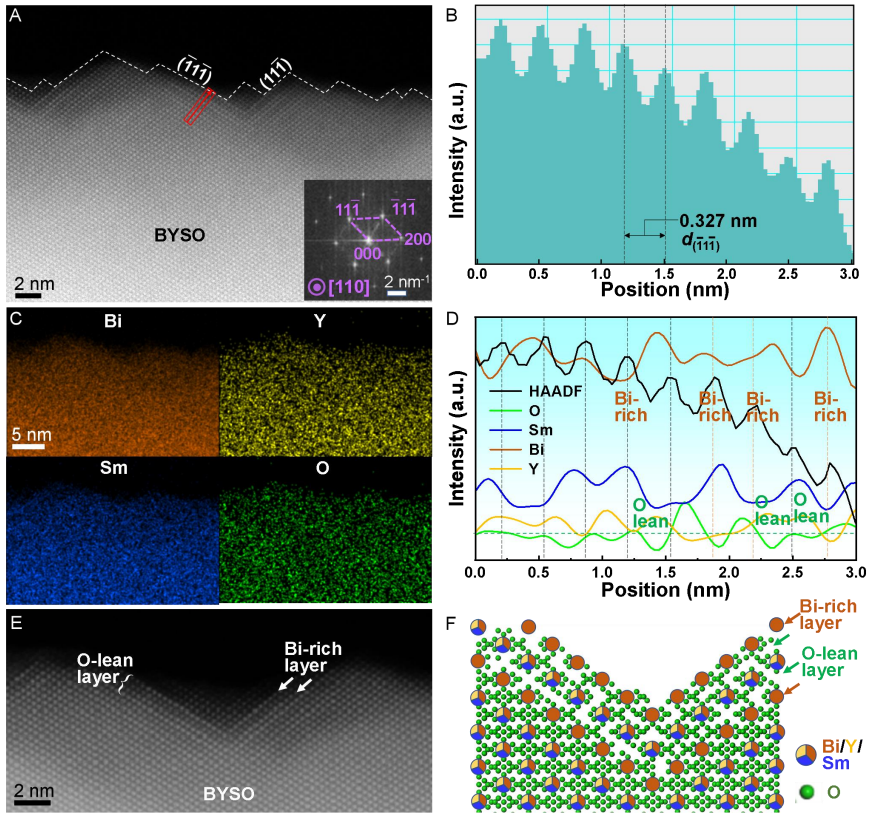

Figure 5. Superficial structure observed along the [110] orientation of the BYSO. (A) Atomic-scale HAADF image. Inset is the indexed FFT of the HAADF image; (B) Intensity line profile from red rectangle overlaid area in (A); (C) Corresponding EDS elemental mappings of (A); (D) Concentration line profiles from red rectangle overlaid area in (A); (E) Locally enlarged surface structure of (A); (F) Proposed atomic model of surface structure.

Theoretical properties of BYSO oxide

DFT calculations were employed to obtain relaxed structures, optical bandgaps, and electronic charge densities for the materials. BYO crystallizes in the $Fm\bar{3}m$ cubic space group with a fluorite-like structure. Figure 6A-D displays the symmetric crystal structures of $Bi_3Y_{1-x}Sm_xO_6$ electrolyte samples. Two inequivalent sites are observed, indicating that Y^{3+} is bonded to six equivalent O^{2-} atoms in a distorted octahedral geometry. At the second site, Sm^{3+} is bound to six oxygen atoms in the doped materials. All Y-O bond lengths are 2.29 Å, and Sm-O bond lengths vary from 2.29 to 2.32 Å. Similarly, Bi^{3+} is bonded to four O^{2-} atoms in a distorted coordination geometry due to

stereoactive lone pair having Bi-O bond distances ranging from 2.23 to 2.63 Å. Due to its relatively large ionic radius, Sm/Y^{3+} typically adopts coordination numbers of six or more in the $Fm\bar{3}m$ oxide systems. For Sm/Y^{3+} to achieve the octahedral coordination proposed for the parent compound δ-Bi_3YO_6, the O3:Y ratio must be at least 1.0, since each oxide ion at an O3 site could be shared by two Sm/Y^{3+} cations under clustered arrangements. However, if Sm^{3+} is assumed to be coordinated exclusively by oxide ions at O3 sites, the remaining oxide ions at these sites are insufficient to meet the coordination requirements of Y^{3+} in the same structural model. Nevertheless, a distorted octahedral environment around Y^{3+} remains feasible, either with one oxide ion at an O3 site and five at O2 sites, or with all six oxide ions located at O2 sites. If the proposed tetrahedral and octahedral geometries for Sm and Y^{3+} are valid, the remaining oxide ions must then coordinate with Bi, in agreement with the well-known stereochemical activity of the Bi $6s^2$ lone pair, which produces asymmetric coordination environments. There are three inequivalent O^{2-} sites. In the first O^{2-} site, O^{2-} is bonded to one Y^{3+} and three equivalent Bi^{3+} atoms to form a combination of distorted edge and corner-sharing $OYBi_3$ trigonal pyramids. The second and third O^{2-} sites are bonded to one Y^{3+}/Sm^{3+} and three equivalent Bi^{3+} atoms to form a fusion of distorted edge and corner-sharing $OYBi_3$ trigonal pyramids. BYO can be regarded as a Y_2O_3-stabilized derivative of Bi_2O_3, especially for the high-temperature δ-Bi_2O_3 fluorite-type oxide family, inherently with a highly defective, dynamically disordered oxygen sublattice. The incorporation of Y^{3+} acts as a stabilizing gene that stabilizes the high-temperature δ-Bi_2O_3 fluorite framework into a wider temperature range, while maintaining a high concentration of mobile oxygen vacancies. Thus, BYO may be regarded as a Y_2O_3-stabilized Bi_2O_3-derived defective fluorite oxide, in which structural stabilization and vacancy-mediated oxide-ion transport are genetically coupled[66]. Sm^{3+} does not simply “dope” BYO; it edits the defective-fluorite genome by reshaping the local coordination environment around oxygen vacancies, thereby changing the admitted oxide-ion migration landscape.

We used the Murnaghan state equation to determine the state characteristics, describing how a body's volume responds to pressure and how far the system is from equilibrium[67]. This state equation is one of many in shock physics and earth sciences that model the behavior of matter under severe pressure. It bears Francis D.'s name. The equation is written as:

$$E(V)=E_0+\left[\frac{\left(\frac{V_0}{V}\right)^{B_0'}}{B_0'-1}+1\right]-\frac{B_0V_0}{B_0-1} \quad (1)$$

Where V_0 is the reference volume, and V is the deformed volume. B_0' is the derivative of the bulk modulus with respect to pressure, *and* B_0 is the bulk modulus. The volume at which the energy is minimal indicates that, for larger volumes, the energy increases; this is the optimized equilibrium energy, confirming that the system is in equilibrium. Figure 6E-F and Supplementary Figure 6 displayed volume optimization plots of $Bi_3Y_{1-x}Sm_xO_6$ (x = 0.00, 0.05, 0.10, 0.20, 0.30) ceramic samples by the Murnaghan equation of state.

Most of the physical properties of solids are related to their band structure. As such, the characteristics and levels of the electronic bandgap primarily determine the semiconductors' optical properties. The optical band structure is calculated using strong symmetry along the lattice's first Brillouin zone (BZ). The features of the energy band structure of the BYSO were shown in Figure 6G, while for other ceramic samples, $Bi_3Y_{1-x}Sm_xO_6$, were shown in Supplementary Figure 7, which indicates the bandgaps in the 1.0-2.0 eV range. Direct bandgap materials, also known as active semiconductors, were suggested by observing the conduction band minimum (CBM) and valence band maximum (VBM) at a point in the BZ. Analyzing the band structures of these compounds reveals that their VBM and CBM are situated at the Γ-symmetry point. Indirect-bandgap optical excitation responded very weakly, particularly near the absorption threshold. The optical band gap of $Bi_3Y_{1-x}Sm_xO_6$ (x = 0.00, 0.05, 0.10, 0.20, 0.30) decreased when the Sm doping ratio increased to x = 0.20 and then started

increasing for x = 0.30. As a result, the direct bandgap BYSO sample possesses smallest band gap compared with other $Bi_3Y_{1-x}Sm_xO_6$ samples.

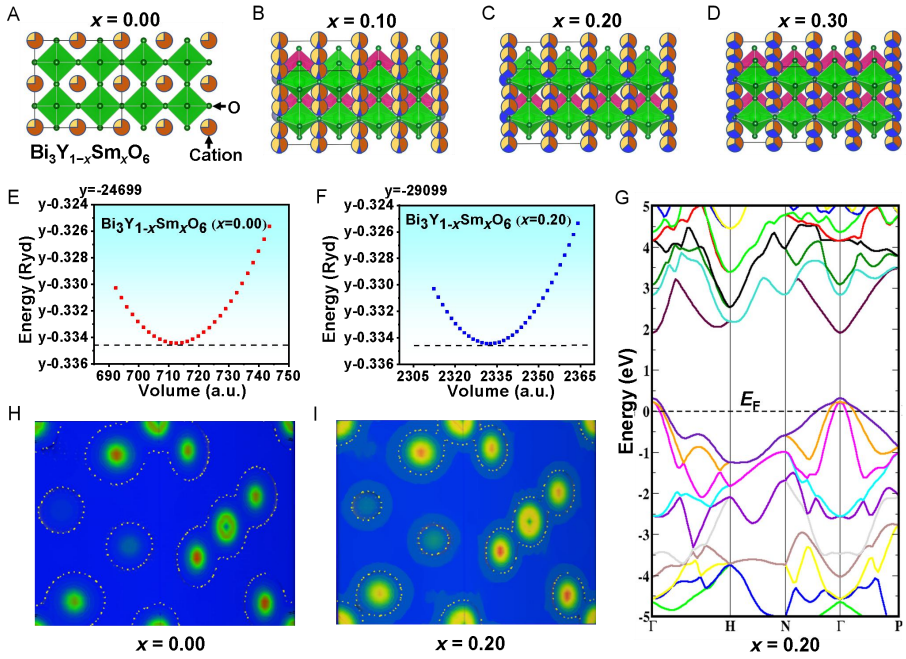

Figure 6. First-principles calculations of the $Bi_3Y_{1-x}Sm_xO_6$ structures. (A-D) Symmetric crystal structures of $Bi_3Y_{1-x}Sm_xO_6$ (x = 0.00, 0.10, 0.20, 0.30) samples along the (100) dimension; (E) and (F) Volume optimization plots of BYO and BYSO by the Murnaghan equation of state; (G) Energy band structure of BYSO by modified Becke-Johnson approximations; (H-I) Electronic charge density of BYO and BYSO unit cells along (100) plane direction.

The estimated differential charge density of the unit cell provides a visual picture of the bonding characteristics and electron transit between atoms. The electronic charge density of BYO and BYSO unit cells were displayed in Figure 6H and I. Other electronic charge densities of $Bi_3Y_{1-x}Sm_xO_6$ (x = 0.05, 0.10, 0.30) can be found in Supplementary Figure 8. The green and red lines denote a decrease, while the yellow line represents an increase in low electron-gaining and probable electron-losing tendency. As a consequence, the strong electron-losing tendency of atomic Bi/Y, and the high electron-shedding tendency of atomic O, could all be indicators of possible interpretations. In contrast to the weak chemical interactions formed by Sm-O, the couple generates remarkably persistent chemical bonds. The figure shows the number

of electrons lost (blue) and the number of electrons added (red) on the scale bar. The rule of thumb is that the more electrons are traded, the darker the color. The electron cloud surrounding the Sm atom exhibits highly polarized characteristics. According to the electronegativity system, which classifies atoms by their tendency to attract electrons, oxygen atoms can lose electrons rapidly and efficiently. Still, Sm atoms are not very good at attracting them, which would lead to the generation of O vacancies. Because electrostatic attraction and repulsion centers do not align, a solid polar covalent connection is formed around the Bi and O atoms. Charge distributions are nearly spherical, and the Sm/Y atom is more ionized and distinct than the other atom, which may explain the enhanced ionic conduction in the material.

CONCLUSIONS

In summary, a pure BYSO oxide solid electrolyte with well-defined, uniformly distributed particles has been successfully fabricated via compositional optimization and a simple solid-state reaction. The obtained BYSO oxide exhibits excellent electrical conductivity of 4.86×10^{-5} S/cm at 300 ºC and 8.1×10^{-2} S/cm at 600 ºC. Furthermore, SOFCs fabricated with the optimal BYSO electrolyte deliver a significant power density of 587 mW/cm^2 and an ionic conductivity of 0.1 S/cm at 550 °C with an open-circuit voltage exceeding 1.0 V under a reduced H_2/air atmosphere. Thus, BYSO constitutes an essential class of oxide ionic conductors with potential applications in various energy-related technologies. Multiple microstructural characterization (STEM-HAADF/EDS, XPS, and theoretical calculations) confirms that the high ion conductivity of the BYSO is related to an increase in oxygen ion vacancy induced by both partial Sm occupation at the distorted octahedral interstitial (namely Frenkel defect) and Sm doping-induced surface reconstruction at $\{111\}_{BYSO}$ crystallographic planes. Elevated O ion mobility by octahedral interstitial Sm, narrow bandgap, and highly ionized Sm/Y atoms also contribute to the high ion conductivity of the BYSO.

DECLARATIONS

Authors' contributions

Conceptualization, methodology, investigation, formal analysis and writing (first draft): A.S, Z.D;

Data provision, investigation, validation, formal analysis: Z.S, Q.M, H.A, W.Q, R.R,

G.M, S.N;

Data verification, review and editing, manuscript revision: W.S.

Availability of data and materials

The original contributions presented in this study are included in the article/Supplementary Materials. Further inquiries can be directed to the corresponding author(s).

AI and AI-assisted tools Statement

Not applicable.

Financial support and sponsorship

This work was supported by the Natural Science Foundation of China (Grant Nos. 52561007, 22175150) and the Natural Science Foundation of Yunnan Province (Grant No. 202301AT070209).

Conflicts of interest

All authors declared that there are no conflicts of interest.

Ethical approval and consent to participate

Not applicable.

Consent for publication

Not applicable.

REFERENCES

1. Ye, W.; Hu, Q.; Zhao, H.; et al., *In situ* reconstruction of proton conductive electrolyte from self-assembled perovskite oxide-based nanocomposite for low temperature ceramic fuel cells. *Chem. Eng. J.* **2024**, *497*, 154977.[DOI: 10.1016/j.cej.2024.154977]

2. Rauf, S.; Hanif, M. B.; Tayyab, Z.; et al., Alternative Strategy for Development of Dielectric Calcium Copper Titanate-Based Electrolytes for Low-Temperature Solid Oxide Fuel Cells. *Nano-Micro Lett.* **2024**, *17*, 13.[DOI: 10.1007/s40820-024-01523-0]

3. Liu, F.; Deng, H.; Diercks, D.; et al., Lowering the operating temperature of protonic ceramic electrochemical cells to < 450 °C. *Nat. Energy* **2023**, *8*, 1145-57.[DOI: 10.1038/s41560-023-01350-4]

4. Xie, J. Prospects of materials genome engineering frontiers. *Mat. Gen. Eng. Adv.* **2023**, *1*, e17.[DOI: 10.1002/mgea.17]

5. Wang, N.; Huang, Z.-Y.; Tang, C.-M.; et al., Functional layer engineering to improve performance of protonic ceramic fuel cells. *Rare Met.* **2023**, *42*, 2250-60.[DOI: 10.1007/s12598-022-02257-x]

6. Raza, R.; Zhu, B.; Rafique, A.; et al., Functional ceria-based nanocomposites for advanced low-temperature (300-600 °C) solid oxide fuel cell: A comprehensive review. *Mater. Today Energy* **2020**, *15*, 100373.[DOI: 10.1016/j.mtener.2019.100373]

7. Guo, X.; Peng, Q.; Shin, K.; et al., Construction of a Composite Sn-DLC Artificial Protective Layer with Hierarchical Interfacial Coupling Based on Gradient Coating Technology Toward Robust Anodes for Zn Metal Batteries. *Adv. Energy Mater.* **2024**, *n/a*, 2402015.[DOI: 10.1002/aenm.202402015]

8. Perrichon, A.; Koza, M. M.; Evenson, Z.; et al., Proton Diffusion Mechanism in Hydrated Barium Indate Oxides. *Chem. Mater.* **2023**, *35*, 6713-25.[DOI: 10.1021/acs.chemmater.3c00754]

9. Xu, D.; Zhang, Q.; Huo, X.; et al., Advances in data-assisted high-throughput computations for material design. *Mat. Gen. Eng. Adv.* **2023**, *1*, e11.[DOI: 10.1002/mgea.11]

10. Yang, X.; Fernández-Carrión, A. J.; Wang, J.; et al., Cooperative mechanisms of oxygen vacancy stabilization and migration in the isolated tetrahedral anion Scheelite structure. *Nat. Commun.* **2018**, *9*, 4484.[PMID: 30367043 PMCID: PMC6203716 DOI: 10.1038/s41467-018-06911-w]

11. Hibino, K.; Tanaka, M.; Kozakai, S.; et al. Experimental visualization of the interstitialcy diffusion of anions in the LaOF-based oxyfluoride $La_{0.9}Sr_{0.1}O_{0.45}F_2$. *ACS Appl. Energy Mater.* **2021**, *4*, 8891-900.[DOI: 10.1021/acsaem.1c01097]

12. Li, J.; Pan, F.; Geng, S.; et al., Modulated structure determination and ion transport mechanism of oxide-ion conductor $CeNbO_{4+\delta}$. *Nat. Commun.* **2020**, *11*, 4751.[PMID: 32958759 PMCID: PMC7506534 DOI: 10.1038/s41467-020-18481-x]

13. Murakami, T.; Shibata, T.; Yasui, Y.; et al., High Oxide-Ion Conductivity in a Hexagonal Perovskite-Related Oxide $Ba_7Ta_{3.7}Mo_{1.3}O_{20.15}$ with Cation Site Preference and Interstitial Oxide Ions. *Small* **2022**, *18*, 2106785.[PMID: 34923747 DOI: 10.1002/smll.202106785]

14. Goodenough, J. B. Oxide-ion conductors by design. *Nature* **2000**, *404*, 821-3.[PMID: 10786774 DOI: 10.1038/35009177]

15. Yashima, M.; Ishimura, D. Crystal structure and disorder of the fast oxide-ion conductor cubic Bi_2O_3. *Chem. Phys. Lett.* **2003**, *378*, 395-9.[DOI: 10.1016/j.cplett.2003.07.014]

16. Kluczny, M.; Song, J. T.; Akbay, T.; et al., Sillén–Aurivillius phase bismuth niobium oxychloride, Bi_4NbO_8Cl, as a new oxide-ion conductor. *J. Mater. Chem. A* **2022**, *10*, 2550-8.[DOI: 10.1039/D1TA07335D

17. Bhattacharyya, R.; Das, S.; Omar, S. Long-term conductivity stability of acceptor-doped $Na_{0.54}Bi_{0.46}TiO_{3-\delta}$. *Solid State Ion.* **2019**, *330*, 40-6.[DOI: 10.1016/j.ssi.2018.12.009]

18. Abrahams, I.; Krok, F. Defect chemistry of the BIMEVOXes. *J. Mater. Chem.* **2002**, *12*, 3351-62.[DOI: 10.1039/B203992N]

19. Dziegielewska, A.; Malys, M.; Wrobel, W.; et al., $Bi_2V_{1-x}(Mg_{0.25}Cu_{0.25}Ni_{0.25}Zn_{0.25})_xO_{5.5-3x/2}$: A high entropy dopant BIMEVOX. *Solid State Ion.* **2021**, *360*, 115543.[DOI: 10.1016/j.ssi.2020.115543]

20. Pirovano, C.; Steil, M. C.; Capoen, E.; et al., Impedance study of the microstructure dependence of the electrical properties of BIMEVOXes. *Solid State Ion.* **2005**, *176*, 2079-83.[DOI: 10.1016/j.ssi.2004.06.026]

21. Yashima, M.; Ishimura, D. Visualization of the diffusion path in the fast oxide-ion conductor $Bi_{1.4}Yb_{0.6}O_3$. *Appl. Phys. Lett.* **2005**, *87*, 221909.[DOI: 10.1063/1.2137894]

22. Abrahams, I.; Liu, X.; Hull, S.; et al., A combined total scattering and simulation approach to analyzing defect structure in Bi_3YO_6. *Chem. Mater.* **2010**, *22*, 4435-45.[DOI: 10.1021/cm101130a]

23. Krynski, M.; Wrobel, W.; Mohn, C. E.; et al., Trapping of oxide ions in δ-Bi_3YO_6. *Solid State Ion.* **2014**, *264*, 49-53.[DOI: 10.1016/j.ssi.2014.06.019]

24. Boyapati, S.; Wachsman, E. D.; Chakoumakos, B. C. Neutron diffraction study of occupancy and positional order of oxygen ions in phase stabilized cubic bismuth oxides. *Solid State Ion.* **2001**, *138*, 293-304.[DOI: 10.1016/S0167-2738(00)00792-X]

25. Wachsman, E. D.; Boyapati, S.; Kaufman, M. J.; et al., Modeling of ordered structures of phase-stabilized cubic bismuth oxides. *J. Am. Ceram. Soc.* **2000**, *83*, 1964-8.[DOI:10.1111/j.1151-2916.2000.tb01498.x]

26. Battle, P. D.; Catlow, C. R. A.; Moroney, L. M. Structural and dynamical studies of δ-Bi2O3 oxide-ion conductors: II. A structural comparison of $(Bi_2O_3)_{1-x}(M_2O_3)_x$ for M = Y, Er, and Yb. *J. Solid State Chem.* **1987**, *67*, 42-50.[DOI: 10.1016/0022-4596(87)90336-7]

27. Borowska-Centkowska, A.; Leszczynska, M.; Wrobel, W.; et al., Structure and conductivity in tungsten doped δ-Bi_3YO_6. *Solid State Ion.* **2017**, *308*, 61-7.[DOI: 10.1016/j.ssi.2017.06.001]

28. Leszczynska, M.; Holdynski, M.; Krok, F.; et al., Structural and electrical properties of $Bi_3Nb_{1-x}Er_xO_{7-x}$. *Solid State Ion.* **2010**, *181*, 796-811.[DOI: 10.1016/j.ssi.2010.04.012]

29. Leszczynska, M.; Borowska-Centkowska, A.; Malys, M.; et al., The double rare-earth substituted bismuth oxide system $Bi_3Y_{1-x}Yb_xO_6$. *Solid State Ion.* **2015**, *269*, 37-43.[DOI: 10.1016/j.ssi.2014.11.012]

30. Asif, S. U.; Wang, J.; Qian, Y.; et al., Phonon vibrations and photoluminescence emissions and their correlations with the electrical properties in Er3+ doped Bi_3YO_6 oxide-ion conductors. *Solid State Ion.* **2020**, *344*, 115092.[DOI: 10.1016/j.ssi.2019.115092]

31. Rasul, M. N.; Anam, A.; Sattar, M. A.; et al., DFT based structural, electronic and optical properties of $B_{1-x}In_xP$(x=0.0,0.25,0.5,0.75,1.0) compounds: PBE-GGA vs. mBJ-approaches. *Chin. J. Phys.* **2018**, *56*, 2659-72.[DOI: 10.1016/j.cjph.2018.10.022]

32. Radzwan, A.; Ahmed, R.; Shaari, A.; et al., First-principles calculations of the stibnite at the level of modified Becke–Johnson exchange potential. *Chin. J. Phys.* **2018**, *56*, 1331-44.[DOI: 10.1016/j.cjph.2018.03.005]

33. Petkov, V.; Maswadeh, Y.; Vargas, J. A.; et al., Deviations from Vegard's law and evolution of the electrocatalytic activity and stability of Pt-based nanoalloys inside fuel cells by in operando X-ray spectroscopy and total scattering. *Nanoscale* **2019**, *11*, 5512-25.[DOI: 10.1039/C9NR01069F]

34. Krynski, M.; Wrobel, W.; Dygas, J. R.; et al., Ab-initio molecular dynamics simulation of δ-Bi_3YO_6. *Solid State Ion.* **2013**, *245-246*, 43-8.[DOI: 10.1016/j.ssi.2013.05.015]

35. Baidya, T.; Bera, P.; Kröcher, O.; et al., Understanding the anomalous behavior of Vegard's law in $Ce_{1-x}M_xO_2$ (M = Sn and Ti; $0 < x \leq 0.5$) solid solutions. *Phys. Chem. Chem. Phys.* **2016**, *18*, 13974-83.[PMID: 27150335 DOI: 10.1039/c6cp01525e]

36. Wang, J.; Gao, D.; Liu, H.; et al., Equivalent circuit modeling on defect-dipole enhanced dielectric permittivity. *J. Mater. Chem. C.* **2020**, *8*, 13235-43.[DOI: 10.1039/D0TC03308A]

37. Sajjad, M.; Asif, S. U.; Guan, L.; et al., Bismuth Yttrium Oxide (Bi3YO6), A new electrode material for asymmetric aqueous supercapacitors. *J. Inorg. Organomet. Polym. Mater.* **2021**, *31*, 1260-70.[DOI: 10.1007/s10904-020-01778-1]

38. Verkerk, M. J.; Keizer, K.; Burggraaf, A. J. High oxygen ion conduction in sintered oxides of the Bi_2O_3-Er_2O_3 system. *J. Appl. Electrochem.* **1980**, *10*, 81-90.[DOI: 10.1007/BF00937342]

39. Umaralikhan, L.; Jaffar, M. J. M. Green synthesis of ZnO and Mg doped ZnO nanoparticles, and its optical properties. *J. Mater. Sci.: Mater. Electron.* **2017**, *28*, 7677-85.[DOI: 10.1007/s10854-017-6461-1]

40. Belostotsky, V. Defect model for the mixed mobile ion effect. *J. Non-Cryst. Solids* **2007**, *353*, 1078-90.[DOI: 10.1016/j.jnoncrysol.2006.12.027]

41. Navrotsky, A. Thermodynamics of solid electrolytes and related oxide ceramics based on the fluorite structure. *J. Mater. Chem.* **2010**, *20*, 10577-87.[DOI: 10.1039/C0JM01521K]

42. Lacorre, P.; Goutenoire, F.; Bohnke, O.; et al., Designing Fast Oxide-Ion Conductors Based on $La_2Mo_2O_9$. *Nature* **2000**, *404*, 856-8.[PMID: 10786788 DOI: 10.1038/35009069]

43. Mushtaq, N.; Lu, Y.; Xia, C.; et al., Promoted electrocatalytic activity and ionic transport simultaneously in dual functional $Ba_{0.5}Sr_{0.5}Fe_{0.8}Sb_{0.2}O_{3-\delta}$-$Sm_{0.2}Ce_{0.8}O_{2-\delta}$ heterostructure. *Appl. Catal. B: Environ.* **2021**, *298*, 120503.[DOI: 10.1016/j.apcatb.2021.120503]

44. Li, M.; Pietrowski, M. J.; De Souza, R. A.; et al., A family of oxide ion conductors based on the ferroelectric perovskite $Na_{0.5}Bi_{0.5}TiO_3$. *Nat. Mater.* **2014**, *13*, 31-5.[DOI: 10.1038/nmat3782]

45. Fop, S.; McCombie, K. S.; Wildman, E. J.; et al., Hexagonal perovskite derivatives: a new direction in the design of oxide ion conducting materials. *Chem. Commun. (Cambridge, U K)* **2019**, *55*, 2127-37.[DOI: 10.1039/C8CC09534E]

46. Fujii, K.; Esaki, Y.; Omoto, K.; et al., New Perovskite-Related Structure Family of Oxide-Ion Conducting Materials $NdBaInO_4$. *Chem. Mater.* **2014**, *26*, 2488-91.[DOI: 10.1021/cm500776x]

47. Karaca, T.; Altınçekiç, T. G.; Faruk Öksüzömer, M. Synthesis of nanocrystalline samarium-doped CeO_2 (SDC) powders as a solid electrolyte by using a simple solvothermal route. *Ceram. Int.* **2010**, *36*, 1101-7.[DOI: 10.1016/j.ceramint.2009.12.005]

48. Prasad, D. H.; Son, J. W.; Kim, B. K.; et al., Synthesis of nano-crystalline $Ce_{0.9}Gd_{0.1}O_{1.95}$ electrolyte by novel sol–gel thermolysis process for IT-SOFCs. *J. Eur. Ceram. Soc.* **2008**, *28*, 3107-12.[DOI: 10.1016/j.jeurceramsoc.2008.05.021]

49. Sharif, M. S.; Rauf, S.; Raza, R.; et al., Semiconductor ionic Cu doped CeO_2 membrane fuel cells. *Ceram. Int.* **2024**, *50*, 40350-62.[DOI: 10.1016/j.ceramint.2024.04.330]

50. Xing, Y.; Wu, Y.; Li, L.; et al., Proton Shuttles in $CeO_2/CeO_{2-\delta}$ Core–Shell Structure. *ACS Energy Lett.* **2019**, *4*, 2601-7.[DOI: 10.1021/acsenergylett.9b01829]

51. Yousaf Shah, M. A. K.; Lu, Y.; Mushtaq, N.; et al., Doped ceria electrolyte rich in oxygen vacancies for boosting the fuel cell performance of LT-CFCs. *Int. J. Hydrogen Energy* **2023**, *48*, 12474-84.[DOI: 10.1016/j.ijhydene.2022.12.153]

52. Zhang, X.; Zhu, L.; Hou, Q.; et al., Toward a consistent prediction of defect chemistry in CeO_2. *Chem. Mater.* **2023**, *35*, 207-27.[PMID: 36644213 PMCID: PMC9835833 DOI: 10.1021/acs.chemmater.2c03019]

53. Wei, W.; Mushtaq, N.; Lu, Y.; et al., Designing composite $BaCe_{0.4}Zr_{0.4}Y_{0.1}Yb_{0.1}O_{3-\delta}$-$Sm_{0.2}Ce_{0.8}O_{2-\delta}$ heterostructure electrolyte for low-temperature ceramic fuel cell (LT-CFCs). *Crystals* **2023**, *13*, 41.[DOI: 10.3390/cryst13010041]

54. Murakami, T.; Hester, J. R.; Yashima, M. High proton conductivity in $Ba_5Er_2Al_2ZrO_{13}$, a hexagonal perovskite-related oxide with intrinsically oxygen-deficient layers. *J. Am. Chem. Soc.* **2020**, *142*, 11653-7.[DOI: 10.1021/jacs.0c02403]

55. Wei, T.; Zhang, L. A.; Chen, Y.; et al., Promising Proton Conductor for Intermediate-Temperature Fuel Cells: $Li_{13.9}Sr_{0.1}Zn(GeO_4)_4$. *Chem. Mater.* **2017**, *29*, 1490-5.[DOI: 10.1021/acs.chemmater.6b03471]

56. Pergolesi, D.; Fabbri, E.; D'Epifanio, A.; et al., High proton conduction in grain-boundary-free yttrium-doped barium zirconate films grown by pulsed laser deposition. *Nat. Mater.* **2010**, *9*, 846-52.[PMID: 20852619 DOI: 10.1038/nmat2837]

57. Yu, Y.; Shah, M. A. K. Y.; Wang, H.; et al., Synergistic Proton and Oxygen Ion Transport in Fluorite Oxide-Ion Conductor. *Energy Mater. Adv.* **2024**, *5*, 0081.[DOI: 10.34133/energymatadv.0081]

58. Bibi, B.; Nazar, A.; Zhu, B.; et al., Emerging semiconductor ionic materials tailored by mixed ionic-electronic conductors for advanced fuel cells. *Adv. Powder Mater.* **2024**, *3*, 100231.[DOI: 10.1016/j.apmate.2024.100231]

59. Chen, X.; Wang, B.; Wang, Z.; et al., Unveiling micromechanism of Fe minor addition-induced property degradation of an Al-5.1Cu-0.65 Mg-0.8Mn (wt%) alloy. *Rare Met.* **2025**, *44*, 3496-513.[DOI: 10.1007/s12598-024-03175-w]

60. Wang, S. B.; Pan, C. F.; Wei, B.; et al., Nano-phase transformation of composite precipitates in multicomponent Al-Mg-Si(-Sc) alloys. *J. Mater. Sci. Technol.* **2022**, *110*, 216-26.[DOI: 10.1016/j.jmst.2021.09.037]

61. Ehrhart, P.; Schilling, W. Investigation of interstitials in electron-irradiated aluminum by diffuse-X-ray scattering experiments. *Phys. Rev. B* **1973**, *8*, 2604.[DOI: 10.1103/PhysRevB.8.2604]

62. Wang, S. B.; Chen, J. H.; Yin, M. J.; et al., Double-atomic-wall-based dynamic precipitates of the early-stage S-phase in AlCuMg alloys. *Acta Mater.* **2012**, *60*, 6573-80.[DOI: 10.1016/j.actamat.2012.08.023]

63. Liu, Y.; Shi, Z.; Liang, T.; et al., The mechanism of room-temperature oxidation of a HF-etched $Ti_3C_2T_x$ MXene determined via environmental transmission electron microscopy and molecular dynamics. *InfoMat* **2024**, *6*, e12536.[DOI: 10.1002/inf2.12536]

64. Dong, Z.; Zhang, L.; Wang, S.; et al., Direct visualization of dynamic atomistic processes of Cu_2O crystal growth through gas-solid reaction. *Nano Energy* **2020**, *70*, 104527.[DOI: 10.1016/j.nanoen.2020.104527]

65. Nellist, P. D.; Pennycook, S. J. Incoherent imaging using dynamically scattered coherent electrons. *Ultramicroscopy* **1999**, *78*, 111-24.[DOI: 10.1016/S0304-3991(99)00017-0]

66. Zhu, B. A state-resonant energy transmission law for energy materials and beyond. *Energy Z* **2026**, *2*, 200001.[DOI: 10.20517/energyz.2026.03]

67. Blanco, M. A.; Francisco, E.; Luaña, V.; GIBBS: isothermal-isobaric thermodynamics of solids from energy curves using a quasi-harmonic Debye model. *Comput. Phys. Commun.* **2004**, *158*, 57-72.[DOI: 10.1016/j.comphy.2003.12.001]